

01 Nov 2014

Large-Scale Mechanical Buckle Fold Development and the Initiation of Tensile Fractures

Andreas Eckert

Missouri University of Science and Technology, eckertan@mst.edu

Peter Connolly

Xiaolong Liu

Follow this and additional works at: https://scholarsmine.mst.edu/geosci_geo_peteng_facwork



Part of the [Geophysics and Seismology Commons](#), and the [Numerical Analysis and Scientific Computing Commons](#)

Recommended Citation

A. Eckert et al., "Large-Scale Mechanical Buckle Fold Development and the Initiation of Tensile Fractures," *Geochemistry, Geophysics, Geosystems*, vol. 15, no. 11, pp. 4570-4587, American Geophysical Union, Nov 2014.

The definitive version is available at <https://doi.org/10.1002/2014GC005502>

This Article - Journal is brought to you for free and open access by Scholars' Mine. It has been accepted for inclusion in Geosciences and Geological and Petroleum Engineering Faculty Research & Creative Works by an authorized administrator of Scholars' Mine. This work is protected by U. S. Copyright Law. Unauthorized use including reproduction for redistribution requires the permission of the copyright holder. For more information, please contact scholarsmine@mst.edu.



RESEARCH ARTICLE

10.1002/2014GC005502

Large-scale mechanical buckle fold development and the initiation of tensile fractures

Andreas Eckert¹, Peter Connolly², and Xiaolong Liu¹¹Department of Geosciences and Geological and Petroleum Engineering, Missouri University of Science and Technology, Rolla, Missouri, USA, ²Chevron ETC, Houston, Texas, USA

Key Points:

- Single-layer buckle folds are simulated under realistic stress conditions
- Permeability and overburden thickness are key parameters in the development of tensile stresses
- Tensile stresses in buckle folds are the result of a combination of horizontal compression and erosional unloading

Supporting Information:

- Readme
- Figures S1–S3

Correspondence to:

A. Eckert,
eckertan@mst.edu

Citation:

Eckert, A., P. Connolly, and X. Liu (2014), Large-scale mechanical buckle fold development and the initiation of tensile fractures, *Geochem. Geophys. Geosyst.*, 15, 4570–4587, doi:10.1002/2014GC005502.

Received 16 JUL 2014

Accepted 7 NOV 2014

Accepted article online 14 NOV 2014

Published online 28 NOV 2014

Abstract Tensile failure associated with buckle folding is commonly associated to the distribution of outer arc extension but has also been observed on fold limbs. This study investigates whether tensile stresses and associated failure can be explained by the process of buckling under realistic in situ stress conditions. A 2-D plane strain finite element modeling approach is used to study single-layer buckle folds with a Maxwell viscoelastic rheology. A variety of material parameters are considered and their influence on the initiation of tensile stresses during the various stages of deformation is analyzed. It is concluded that the buckling process determines the strain distribution within the fold layer but is not solely responsible for the initiation of tensile stresses. The modeling results show that tensile stresses are most dependent on the permeability, viscosity, and overburden thickness. Low permeability ($<10^{-19}$ m²), high viscosity ($\geq 10^{21}$ Pa s), and low overburden pressure can explain tensile failure at the fold hinge. Tensile stresses in the limb of the fold cannot (in general) be explained by buckling. Rather, it develops due to a combination of compression and erosional unloading. The modeling results show that erosion of high permeability rocks can explain the generation of tensile stresses at significant depths (~ 2 km) both at the hinge of the fold and throughout the limb of the fold. This study shows that tensile stresses and associated failure within buckle folds is directly dependent on the distribution of material parameters but moreover to the strain history of the geologic system.

1. Introduction

Folds and fold trains of sedimentary strata are among the most common structural trap systems for hydrocarbon reservoirs. The existence and occurrence of natural fracture systems associated with fold structures play an important role in hydrocarbon migration and production since these fractures often behave as zones of elevated permeability [Sibson, 1996]. Of particular interest in a geomechanical analysis of such reservoirs is the prediction of the location, type, extent, and orientation of these fold-related structures both for fluid flow pathway and reservoir stability prediction. The occurrence and development of these fracture systems during fold evolution have been extensively studied and are dependent on a variety of parameters, such as layer thickness [e.g., McQuillan, 1973; Narr and Suppe, 1991; Schmalholz et al., 2002], lithology [e.g., Price, 1974; Ericsson et al., 1998; Bai and Pollard, 2000], rheology [Zhang et al., 1996; Frehner, 2011], elastic property contrasts [Bourne, 2003], the state of stress [Price, 1966; Ramsay, 1967; Stearns, 1968; Price and Cosgrove, 1990; Lemiszki et al., 1994], interlayer slip [Chapple and Spang, 1974; Cooke and Underwood, 2001; Smart et al., 2009], and their position in the fold system [e.g., Price and Cosgrove, 1990].

Several authors [e.g., Price, 1966; Stearns, 1968; Price and Cosgrove, 1990; Bergbauer and Pollard, 2004] have presented a conceptual model of 5–6 different symmetric fracture sets associated to fold structures (Figure 1). In order to predict the occurrence of fold-related fractures, a distinction has to be made relative to the time of their development, i.e., if the fractures have occurred before, during, or after the folding. As Price and Cosgrove [1990] point out, different sets of conjugate shears in an anticline (fracture Sets 1–4 in Figure 1), and tensile fractures perpendicular to the bedding planes and oriented either along or perpendicular to the fold axis (fracture Sets 5–6 in Figure 1) require different relations of the principal stresses, and thus these fractures develop at different times during the deformation history of the fold as the stress state changes.

This paper focuses on the generation of tensile fractures in large-scale buckle folds. Tensile fractures normal to the bedding and parallel to the fold axis are commonly reported as occurring in the outer arc of fold

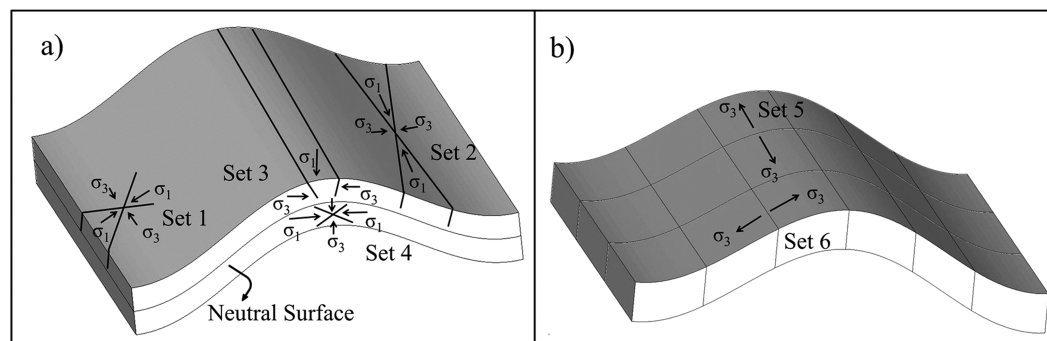


Figure 1. (a) Set of four different shear fractures commonly associated to fold structures. (b) Two sets of extensional fractures associated to fold structures. Figures after Price and Cosgrove [1990].

hinges [Narr and Suppe, 1991; Fischer and Wilkerson, 2000; Hennings et al., 2000; Bergbauer and Pollard, 2004] but field observations also show their occurrence in fold limbs [Silliphant et al., 2002; Reber et al., 2010]. It is generally postulated that these fractures are the result of the buckling processes during the evolution of the geologic structure [Stearns and Friedman, 1972; Srivastava and Engelder, 1990]. This becomes of interest as different studies [Price and Cosgrove, 1990; Twiss and Moores, 2007; Bergbauer and Pollard, 2004] conclude that preexisting vertical joint sets play an important role in the distribution of fold-related fractures. Consequently, the prediction and analysis of folding-related extensional fractures can be separated into studies considering the development of the fold structure and its associated fractures over geologic time scales and into studies which are based on final fold geometry.

A common technique for fracture prediction for developed fold shapes is fold curvature analysis [e.g., Lisle, 1994; Fischer and Wilkerson, 2000; Bergbauer and Pollard, 2004] which assumes that the folded layers represent elastically bent plates and the fractures associated with the fold are a result of the bending strains.

In order to distinguish compressional failure and tensile failure, the neutral surface concept [Ramsay, 1967; Price and Cosgrove, 1990; Twiss and Moores, 2007; Frehner, 2011] is used. The neutral surface of a fold separates regions of layer parallel extensional strain above the surface and layer parallel compressional strain below it. Limitations of fold curvature analysis are that it does not account for the stress differences arising from material heterogeneities, does not account for the changes of the state of stress due to changing pore pressures and does not consider the timing of fracture formation [Smart et al., 2009].

Geomechanical models using finite element analysis (FEA) overcome these drawbacks and enable simulation of the mechanical development of buckle fold trains as a result of the applied stresses and strains over geologic time scales. Numerical modeling techniques have been used as early as 1969 [Dieterich and Carter] to study folding and many studies have been conducted since to provide a more thorough understanding of fold development. It is understood that rheology [e.g., Zhang et al., 1996; Schmalholz and Podladchikov, 1999; Jeng and Huang, 2008; Frehner, 2011], strain rate [Lemiscki et al., 1994; Jeng et al., 2002], kinematic boundary conditions [Schmalholz, 2008], and initial perturbation [Mancktelow, 1999; Zhang et al., 2000] have significant influence on fold geometry and stress and strain distribution.

Several studies have investigated the influence of buckle fold development on the occurrence of associated tensile fractures. Lemiszki et al. [1994] show that, depending on strain rate, the burial depth and the pore pressure distribution have a significant influence on the initiation of hinge parallel extensional fracture sets. Casey and Butler [2004] observe dramatic changes in layer-parallel stresses and argue that various types of failure (tensile, shear, and grain crushing) could be explained by their modeling results. One of their main conclusions is that due to the complexity of stress history of fold hinges the timing of fracturing is not predictable. Reber et al. [2010] employ 3-D viscous FE analysis to study the formation of mode I tensile fractures. They conclude that, based on the history of stress orientations during folding, fractures perpendicular to the fold axis form during small fold amplitudes under layer-subparallel compression, and that fractures parallel to the fold axis are occurring when fold amplitudes are large and fold limbs are under layer-subparallel tension. Frehner [2011] developed a concept of incremental neutral lines (representing zero layer parallel

strain rate) and final neutral lines (representing zero layer parallel strain) during folding and their relationship to fracture initiation. The study shows that tensile fracture initiation and its growth may be related but, due to the influence of overburden and pore pressure, is not directly proportional to the position of the incremental neutral line.

While a great amount of knowledge has been gained on the evolution of folds and their stress and strain history, many assumptions and simplifications are made. Only a few studies consider the influence of gravity [Schmalholz *et al.*, 2002] and the influence of pore pressure/overpressure is often reduced to the analysis of the mean stress [e.g., Stephansson, 1974; Mancktelow, 2008]. The studies discussed above show that the stress history of folding is dependent on many physical parameters and that the prediction of the timing and evolution of the associated fractures requires additional understanding. The particular question that arises is whether tensile fractures are necessarily associated with the stresses and strains occurring as a result of flexural forces during folding. In other words, is the flexure due to buckling the only physical process that produces tensile failure at the hinge and in the limbs of buckle folds? Fehner's [2011] study shows that extensional strains may explain the occurrence of tensile failure, but tensile fractures only form when the minimum effective principal stress exceeds the tensile strength of the rock. However, during the evolution of a fold and its exhumation, conditions for tensile failure can develop which are not directly related to buckling. Thus, field observations from outcrops exhibiting tensile failure may not be a valid sample with which to confirm tensile failure at depth since processes such as uplift and exhumation can also result in rock failure. As Fehner [2011] points out, both overburden and pore pressure have significant influence on the development of tensile fractures. However, to the authors' knowledge, no study comprehensively addresses the formation of fractures related to overburden and fluid pressure. In this context, the material's permeability plays an important role in the generation of compression related overpressures and its potential to generate fractures and a more thorough understanding is necessary.

This study uses 2-D plane strain FEA using viscoelastic rheology to simulate single-layer buckle fold development of one class of sediments under realistic in situ stress and pore pressure conditions. The influence of material parameters, burial depth, permeability, and exhumation are studied to gain a more thorough understanding of the initiation of fold-related tensile fractures. Of particular interest are the specific conditions for the initiation of tensile fracture sets known to occur at depth [Ramsay and Huber, 1987] during the buckling process.

2. Modeling Approach

2.1. Theoretical Background

In this study, viscoelastic single-layer fold systems are simulated and a classic Maxwell model is adopted following the studies of Mancktelow [1999], Zhang *et al.* [2000], and Schmalholz *et al.* [2001]. The Maxwell rheology enables instantaneous elastic behavior for fast strain rates and time-dependent viscous behavior for slower strain rates.

For this study, it is assumed that folds extend infinitely along the fold axis and that the displacements of all points in the model are parallel to the x - z plane. Therefore, a 2-dimensional plane strain approach is followed. In addition to the viscoelastic Maxwell rheology, pore pressure is introduced by utilizing effective stress analysis assuming an incompressible fluid and rock matrix (i.e., Biot coefficient $\alpha=1$; see supporting information). The finite element method (via the commercial software package ABAQUSTM) is employed to solve the equations of equilibrium, conservation of mass, constitutive equations, and the equations for pore fluid flow. The unknowns of the problem comprise the stress tensor components σ_{xx} , σ_{zz} , and σ_{xz} , the pore pressure P_p , the material velocities in x and z directions v_x and v_z , and the material density ρ_m .

The equilibrium equations for plane strain are given by [Jaeger *et al.*, 2007]:

$$\frac{\partial \sigma_{xx}}{\partial x} - \frac{\partial P_p}{\partial x} + \frac{\partial \sigma_{xz}}{\partial z} = 0 \quad (1)$$

$$\frac{\partial \sigma_{zz}}{\partial z} - \frac{\partial P_p}{\partial z} + \frac{\partial \sigma_{xz}}{\partial x} + \rho_m g = 0 \quad (2)$$

The constitutive relationships for a compressible Maxwell body in plane strain are [Ranalli, 1995]:

$$\dot{\epsilon}_{xx} = \frac{1}{3K} \frac{\partial \sigma_{xx}^{iso}}{\partial t} - \frac{\alpha}{3K} \frac{\partial P_p}{\partial t} + \frac{1}{2G} \frac{\partial \sigma_{xx}^{dev}}{\partial t} + \frac{\sigma_{xx}^{dev}}{2\mu} \quad (3)$$

$$\dot{\epsilon}_{zz} = \frac{1}{3K} \frac{\partial \sigma_{zz}^{iso}}{\partial t} - \frac{\alpha}{3K} \frac{\partial P_p}{\partial t} + \frac{1}{2G} \frac{\partial \sigma_{zz}^{dev}}{\partial t} + \frac{\sigma_{zz}^{dev}}{2\mu} \quad (4)$$

$$\dot{\epsilon}_{xz} = \frac{1}{2G} \frac{\partial \sigma_{xz}^{dev}}{\partial t} + \frac{\sigma_{xz}^{dev}}{2\mu} \quad (5)$$

where K is the Bulk modulus, G the Shear modulus, μ the viscosity, and α the Biot coefficient. The superscript “iso” denotes the isotropic part of the stress tensor and “dev” denotes the deviatoric part. Since the material density, ρ_m , in the model is depth dependent and depth changes with time, the conservation of mass is represented as:

$$\frac{\partial \rho_m}{\partial t} + \rho_m \left(\frac{\partial v_x}{\partial x} + \frac{\partial v_z}{\partial z} \right) = 0 \quad (6)$$

Fluid flow is simulated by Darcy’s law [Jaeger et al., 2007] and since assuming $\alpha = 1$ (see supporting information) the governing diffusion equation for the pore pressure is given by:

$$\frac{Kk_x}{\mu_f} \frac{\partial^2 P_p}{\partial x^2} + \frac{Kk_z}{\mu_f} \frac{\partial^2 P_p}{\partial z^2} - \frac{\partial P_p}{\partial t} + \dot{\sigma}^{iso} = 0 \quad (7)$$

where $k_{x,z}$ represents the permeability components, μ_f the fluid (i.e., water) viscosity. Equations (1–7) represent the seven governing equations to solve for the seven unknowns of the problem. The detailed derivation of the equation system can be found in supporting information.

From equation (7), it can be seen that the pore pressure response is coupled to the volumetric strain (and hence to the isotropic stress tensor). Fluid flow is then modeled as the result of strain-related pore volume changes, whereby pore pressure is increased in regions of compressional strain (i.e., reduction in volume) and pore pressure is decreased in regions of extensional strain (i.e., increase in volume).

2.2. Dominant Wavelength

In order to study the stress distribution of buckle folds the numerical models are setup such that only one wavelength is amplified. Based on the classic single-layer fold theory [e.g., Biot, 1961], it has been found that folds are characterized by a dominant wavelength λ_{dv} , which is dependent on the viscosity contrast, R_{μ} , between the competent (to be folded) layer and the surrounding matrix ($\lambda_{dv} = 2\pi \sqrt[3]{\frac{\mu_l}{6\mu_m}}$, where h is the layer thickness, μ_l the folding layer viscosity, and μ_m the matrix viscosity). In order to determine an appropriate dominant wavelength for the various models, the approach by Schmalholz and Podladchikov [1999] and Schmalholz et al. [2001] is followed using the parameter R which determines if the competent layer is folded viscously ($R < 1$) or elastically ($R > 1$). R is defined as the ratio between the viscous dominant wavelength, λ_{dv} , and the elastic dominant wavelength, λ_{de} :

$$R = \frac{\lambda_{dv}}{\lambda_{de}} = \sqrt[3]{\frac{\mu_l}{6\mu_m}} \sqrt{\frac{P_0}{G}} \quad (8)$$

where G is the shear modulus and P_0 is the initial layer parallel stress. For the range of viscosities μ_l (i.e., $5 \times 10^{19} - 5 \times 10^{21}$ Pa s) in the numerical models, the deformation will be dominantly viscous and the initial layer parallel stress is given by $P_0 = 4\mu_l \dot{\epsilon}$ [Schmalholz and Podladchikov, 1999]. Based on these values, the parameter R is calculated for models having a viscosity ratio of 50. The data show that R is in the range of 0.026–0.262 (supporting information Table S1), indicating that deformation is dominated by viscous behavior. Therefore, for these models λ_{dv}/h of 12.74 m is chosen. For the different viscosity ratios, R_{μ} considered (i.e., 20, 100, 200), R is in the range of 0.093–0.186 (supporting information Table S1), and the appropriate λ_{dv}/h is chosen accordingly.

2.3. Model Setup

The geometry of the 2-D finite element model comprises a central single-folding layer 30 m thick embedded in a matrix 2 km thick (Figure 2). The folding layer is characterized by small periodic perturbations of the viscous dominant wavelength and 2.5 m amplitude and is horizontally compressed using a strain rate of 10^{-14} s^{-1} , representative of a reasonable geologic deformation rate [Twiss and Moores, 2007]. The overall horizontal model dimension is 1911 m, enabling several fold trains to develop. The folding layer and matrix

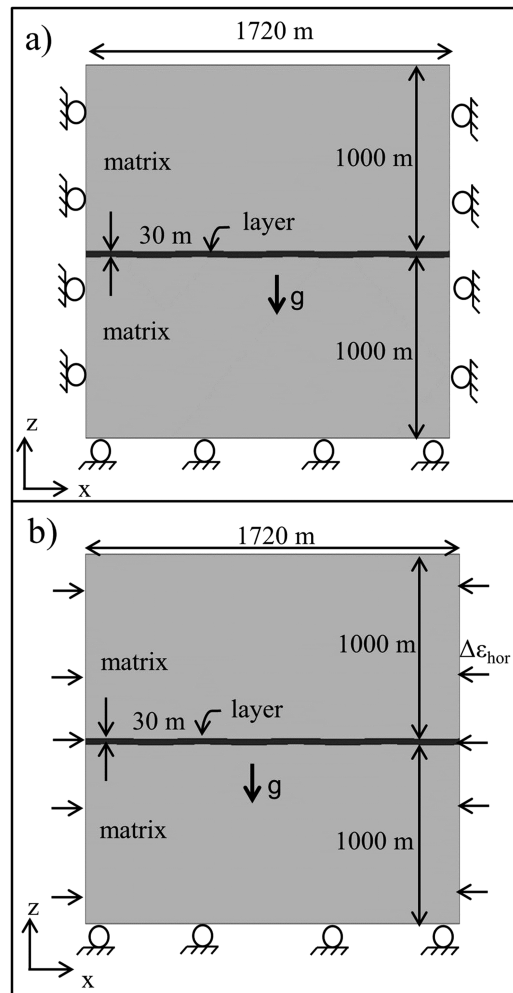


Figure 2. Boundary conditions for 2-D numerical models. (a) In order to simulate realistic stress magnitudes in a numerical model gravitational prestressing is applied. This step utilizes a boundary condition setting where only gravity is acting and the model sides are constrained such that only in-plane displacements are allowed (rollers). The instantaneous gravitational compaction results in a state of stress that is used as initial conditions for subsequent modeling steps. (b) After reaching gravitational equilibrium a constant, tectonic strain ϵ_{hor} can be added to the model, which results in the initiation of buckling.

3. Results

In order to determine the initiation and evolution of tensile fractures, the stress history during the fold development has to be analyzed. In the analysis of the modeling results, the spatial and temporal evolution

Properties	Folding Layer	Matrix
Specific gravity	2.75	2.75
Viscosity	10^{21} (Pa s)	2×10^{19} (Pa s)
Young's modulus	$33.7(1 - 0.1639e^{-0.00039z})$ (GPa)	$3.37(1 - 0.1639e^{-0.00039z})$ (GPa)
Poisson ratio	0.25	0.25
Permeability (at 1000 m)	$1.75 \cdot 10^{-15}$ (m ²)	$1.75 \cdot 10^{-15}$ (m ²)
Strain rate	10^{-14} (s ⁻¹)	10^{-14} (s ⁻¹)

of the minimum effective in-plane principal stress, termed σ'_3 , is used as the main indicator for possible tensile fracture development. This indicator is chosen since tensile failure occurs when σ'_3 equals the tensile strength (T_0) of the rock (i.e., $\sigma'_3 = -T_0$) and thus the timing of σ'_3 meeting this condition during the fold evolution becomes crucial. To simplify the analysis and reduce the need to make assumptions regarding the rocks'

$$\phi(z) = 16.39e^{-0.00039z} \quad (9)$$

where ϕ is the porosity, and z is the depth in m (relative to the top of the matrix).

Because permeability is also a function of depth, the relationship given Medina et al. [2011] is modified to account for lower permeabilities:

$$k(z) = 7.583 \cdot 10^{-17} e^{0.283\phi} \quad (10)$$

where ϕ is the porosity, z is the depth in meter, and k is the permeability in m².

The initial pore pressure distribution in the model is assumed to be hydrostatic and the permeability is considered to be anisotropic with the horizontal permeability being 5 times the vertical permeability. A list of the model material parameters is given in Table 1 wherein the magnitudes of the parameters represent the base case (model) considered.

In order to simulate realistic in situ stress magnitudes in a 2-D or 3-D numerical model, a stress initialization procedure (termed prestressing) is required wherein the modeled stresses generated as a result of gravitational compaction reach a state of equilibrium. A common procedure to simulate realistic in situ stresses involves the following steps [Buchmann and Connolly, 2007; Eckert and Connolly, 2007; Smart et al., 2009] (Figure 2): (1) gravitational prestressing based on the equations of linear elasticity; (2) application of horizontal strain in order to simulate the horizontal compression to initiate buckling. Shortening in the x direction is accomplished by applying a constant strain rate until 50% shortening is reached.

of the minimum effective in-plane principal stress, termed σ'_3 , is used as the main indicator for possible tensile fracture development. This indicator is chosen since tensile failure occurs when σ'_3 equals the tensile strength (T_0) of the rock (i.e., $\sigma'_3 = -T_0$) and thus the timing of σ'_3 meeting this condition during the fold evolution becomes crucial. To simplify the analysis and reduce the need to make assumptions regarding the rocks'

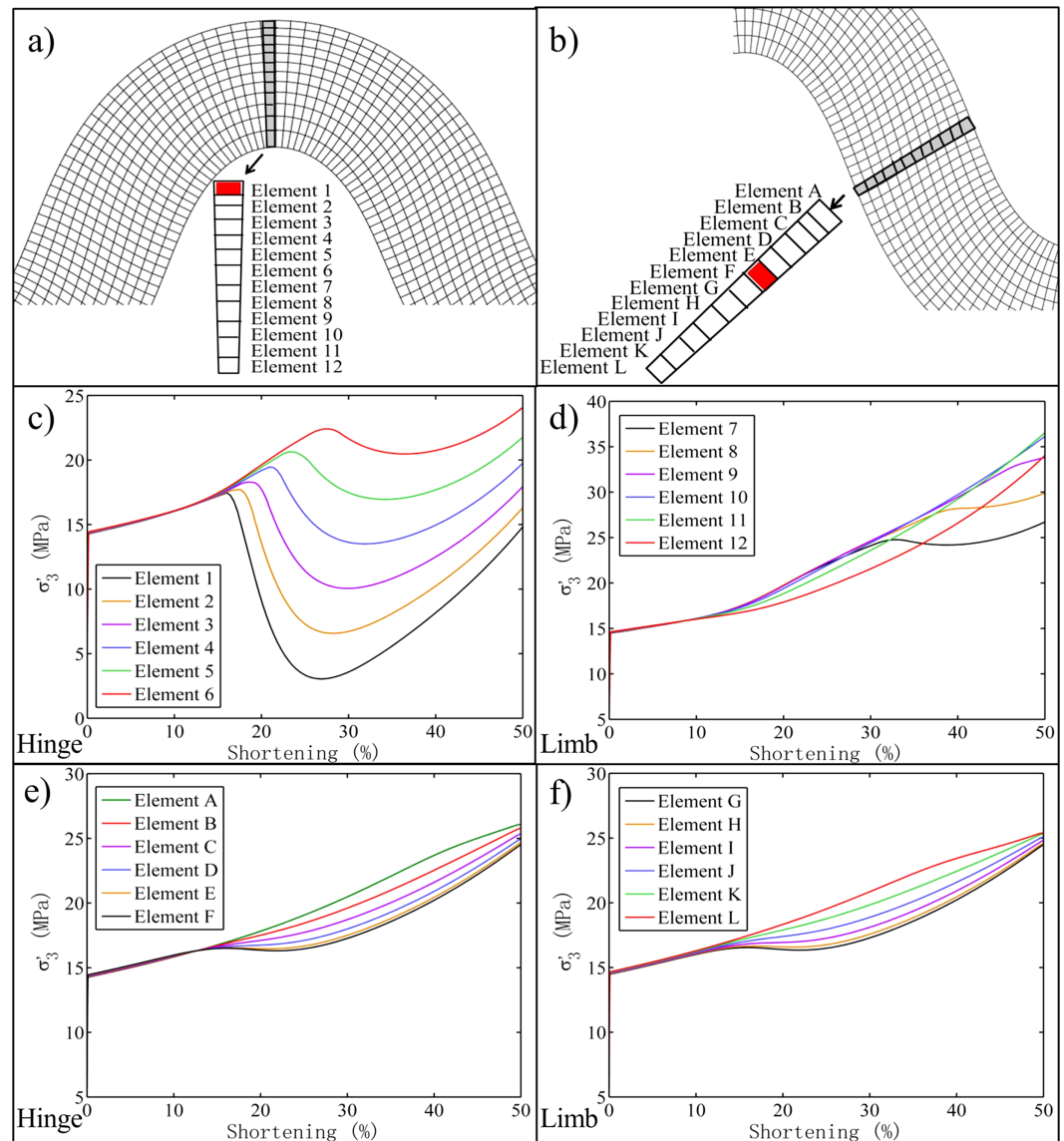


Figure 3. (a) Results for the minimum principal stress are analyzed for Element 1 (red) along the hinge of the fold. (b) Results for the minimum principal stress are analyzed for the central element (F) at the limb of the fold. (c, d) The stress evolution (σ_3) for the hinge of the fold shows the minimum for element 1. (e, f) σ_3 for the limb of the fold shows no significant differences across the layer.

tensile strength, the case where $T_0 = 0$ is considered. Thus, the discussion identifies regions of tensile σ_3 as potential fracturing sites. The following analyses investigate the stress history of the developing fold trains at their hinges (i.e., Element 1 in Figure 3a) as this is the location with the highest probability to reach tensile stresses. As shown for the base case model (Table 1), σ_3 magnitudes initially increase before they steeply drop after $\sim 16\%$ shortening and reach a pronounced minimum at $\sim 26\%$ shortening (Figure 3c). As the strain distribution in single-layer buckle folds is layer parallel, the resulting stress distribution does not vary significantly along a layer perpendicular cross section in the limb (Figures 3e and 3f). Hence, the evolution of σ_3 in the limbs is only presented for element F (Figure 3b highlighted in red color) as it has the lowest value.

Fold systems form in a variety of geologic environments and a series of parametric studies is performed with the aim of providing a better understanding of which conditions are necessary to initiate tensile failure during buckle folding and which parameters have the greatest influence. The parameters considered are overburden thickness, competence contrast, viscosity, and permeability. In each series of analyses, only one parameter is varied. The remaining model parameters of specific gravity, Young's modulus, Poisson's ratio, and strain rate (Table 1) remain constant.

The ratio of P_0/G [Schmalholz and Podladchikov, 1999] (i.e., layer parallel stress over shear modulus) for the various models investigated ranges from ~ 0.0053 (for all models based on Table 1) to ~ 0.021 (for model with highest viscosity). This is within the range of P_0/G results previously reported for viscoelastic buckle folds [Schmalholz and Podladchikov, 1999].

3.1. Parametric Study

3.1.1. Overburden

The amount of initial overburden thickness is increased from 0.5 to 3 km. It is important to note that the overburden depth and the rock density do not remain constant during the development of the fold. As a result of the horizontal compression, significant “thickening” of the model domain occurs and the overburden stress increases. For example, an initial overburden of 500 m results in 978 m of overburden after 50% shortening. As expected, larger overburden thicknesses results in larger vertical stresses and thus a higher degree of compression both at the hinge and the limb of the fold (Figures 4a and 4b). As can be seen for all cases, a steep drop in σ'_3 is observed at the hinge after 16–20% shortening and σ'_3 magnitudes reach a minimum at approximately 25–30% shortening, before σ'_3 magnitudes steadily increase again (Figure 4a). The drop in σ'_3 can be explained by the occurrence of tensile fiber stresses due to the buckling process. The subsequent increase in σ'_3 is explained by the steady increase in overburden pressure in combination with the ongoing horizontal compression. Figure 4a also shows that tensile stresses at the hinge are only obtained for the lowest overburden thickness of 500 m. At the limb of the fold structure (Figure 4b), the σ'_3 magnitudes never become tensional and show comparatively little variation.

3.1.2. Competence Contrast

Figure 4c shows the temporal evolution of the minimum effective principal stress, σ'_3 , at the hinge of the fold structure for models with different competence contrasts ($R_\mu = 25, 50, 100, 200$). The general trend for the σ'_3 magnitude at the hinge of the fold structure shows a continuous increase until at a certain shortening percentage (9–30%) a drop in σ'_3 occurs. For larger values of R_μ , this σ'_3 decline occurs at a lower shortening percentage and the decline is steeper, also reaching lower σ'_3 magnitudes. This behavior reflects the onset of fold amplification after a period of layer parallel compression, which occurs earlier for higher viscosity ratios, as also observed by [Johnson and Fletcher, 1994]. Tensile stress magnitudes are not reached for any of the competence contrasts considered. At the limb of the fold structure (Figure 4d), the σ'_3 magnitudes never become tensional and steadily increase with shortening.

3.1.3. Viscosity

Using a constant competence contrast ($R_\mu = 50$), viscosities for the folding layer are varied from 5×10^{19} Pa s to 10^{21} Pa s which represents a common range for crustal rocks [Twiss and Moores, 2007]. The stress evolution at the hinge (Figure 4e) shows a similar trend for viscosities of 5×10^{19} and 10^{20} Pa s whereby stresses do not vary much between limb and hinge. For higher viscosities, i.e., 5×10^{20} Pa s and above, σ'_3 magnitudes drop after $\sim 16\%$ shortening and become tensile for $\mu_f > 10^{21}$ Pa s. This can be explained by considering the factor R [Schmalholz and Podladchikov, 1999]. R for the high viscosity models (supporting information Table S1) reaches values of ~ 0.31 for the later stages of shortening resulting in a more elastic response compared to the base model for which $R = 0.15$, and thus results in more extreme stress magnitudes. σ'_3 magnitudes on the limb of the fold (Figure 4d) show the same response with respect to viscosity as σ'_3 at the hinge; however, tensile stresses are not obtained.

3.1.4. Permeability

For the permeability analysis, both matrix and folding layer are characterized by the same permeability. It is recalled that the permeability is considered to be anisotropic with the horizontal permeability being 5 times greater than the vertical. Horizontal permeabilities are varied from 10^{-13} m² to 10^{-23} m² reflecting a large range of sedimentary rocks [Jaeger et al., 2007]. Since compression of porous material results in overpressure, the dependence of σ'_3 and the pore pressure with respect to the permeability is analyzed.

Figure 5a shows the evolution of the pore pressure at the hinge during fold formation. For high permeabilities (10^{-13} to 10^{-17} m²), overpressure does not develop and the pore pressure is close to the theoretical hydrostatic value (Figure 5a). For lower permeabilities (10^{-19} to 10^{-23} m²), the folding layer becomes overpressured almost instantaneously after the onset of horizontal compression. In the early stages of the fold development ($< 18\%$ shortening), the lowest permeability results in the highest degree of overpressure. For the later stages ($> 18\%$ shortening), pore pressures steadily increase; however, the maximum pore pressure

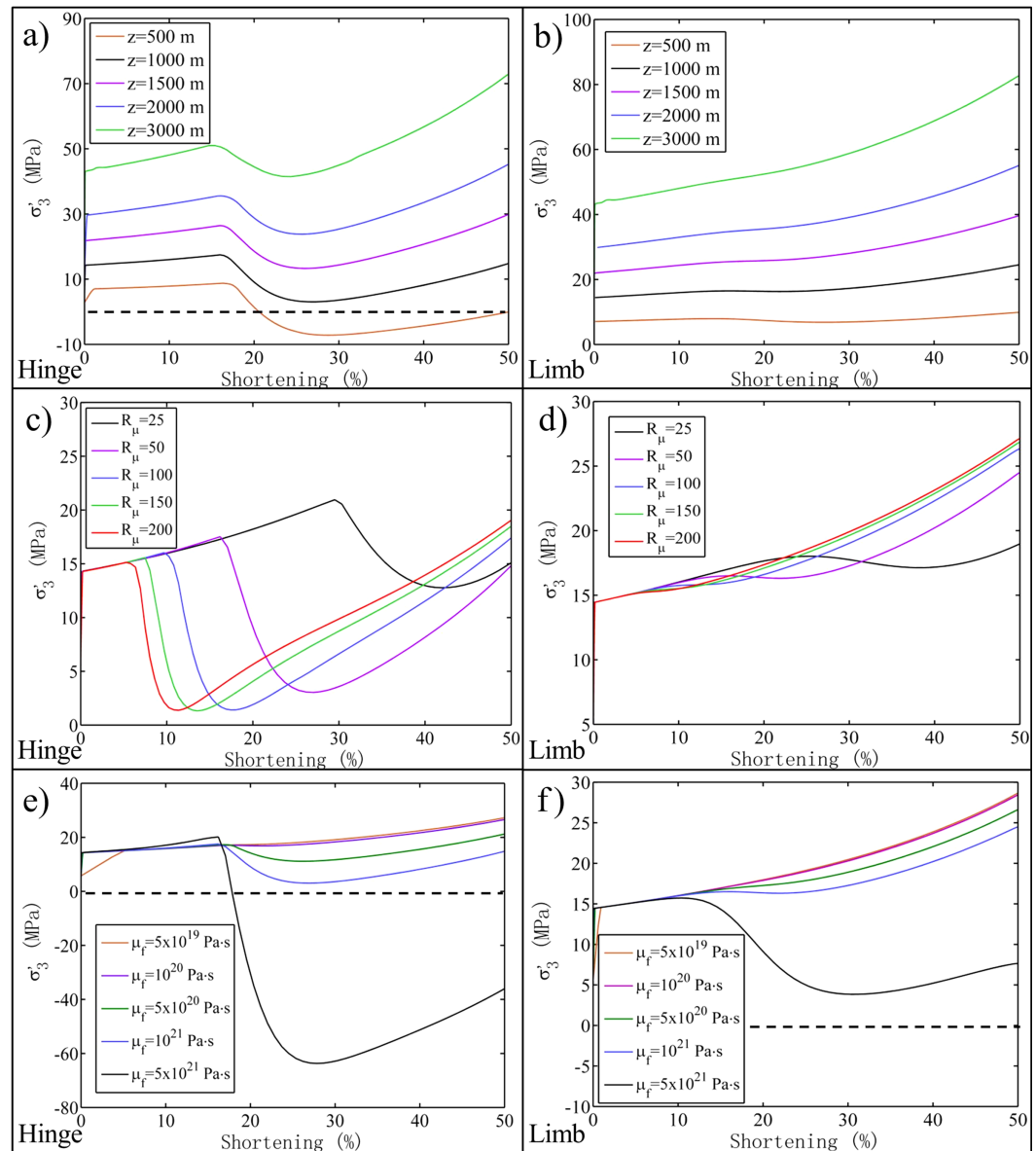


Figure 4. Results of minimum principal stress (σ_3) with respect to model shortening for the various parameters tested. The dashed line at 0 MPa marks the onset of possible tensile failure. (a) σ_3 for various overburden thicknesses at the hinge. The overburden thickness determines the degree of compression of the model and as expected lower overburden thickness results in lower σ_3 magnitudes. For the lowest thickness, tensile stresses occur after $\sim 20\%$ shortening. (b) σ_3 at the limb of the fold do not vary significantly and do not reach tensile magnitudes for any thickness. (c) σ_3 at the hinge of the fold for various competence contrast ratios. The higher the competence contrast between matrix and folding layer the earlier a drop in σ_3 can be observed. (d) σ_3 at the limb of the fold for various competence contrasts shows steady increase with shortening. (e) σ_3 at the hinge of the fold for various viscosities tested. Only for high viscosities ($> 10^{21}$ Pa s), a rapid decrease in σ_3 reaching tensile stresses can be observed. (f) σ_3 at the limb of the fold for various shows a similar behavior but does not reach tensile stress magnitudes.

at the hinge is obtained for $k = 10^{-21} \text{ m}^2$ (Figure 5a) and not for the lowest permeability case. At the limb of the fold, the pore pressure evolution follows the same trend as for the hinge (Figure 5b). This behavior can be explained by the pore pressure evolution (Figure 6). It can be seen that for 10^{-21} m^2 the pore pressure in the folding layer and the matrix are hydraulically connected, resulting in pore pressure magnitudes that correlate to depth (Figure 6a) with the lowest pore pressure of 38.64 MPa occurring at the hinge of the fold and the highest pore pressure of 41.03 MPa at the bottom of the synform. For 10^{-23} m^2 (Figure 6b), the pore pressure in the folding layer and the matrix are slightly decoupled and linked to the strain distribution in the layer, whereby the pore pressure is not depth related and the maximum pore pressure of 41.23 MPa occurs at the limb of the fold. The slightly lower pore pressure at the hinge can be explained by the slightly higher extensional strain developed here.

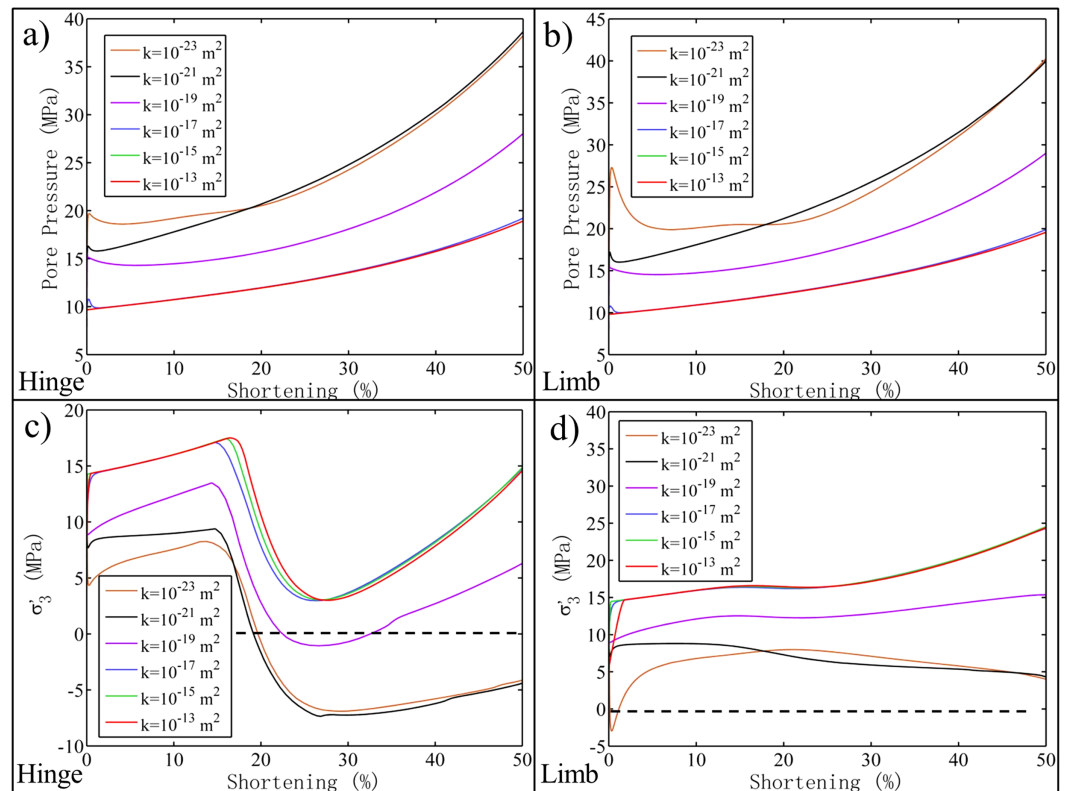


Figure 5. (a) Pore pressure evolution at the fold hinge. Permeabilities of 10^{-13} to 10^{-17} m^2 do not result in overpressure and pore pressure is equivalent to hydrostatic. Lower permeabilities exhibit overpressure, whereby the highest pore pressure at the hinge is obtained for 10^{-21} m^2 . (b) Pore pressure evolution at the fold limb showing the same trend as for the hinge. (c) σ'_3 at the hinge of the fold show a steady increase towards a maximum at ~ 15 – 16% shortening before declining. The steepest decline and hence the lowest stress is observed for 10^{-21} m^2 , reaching tensile stresses (below dashed black line) at $\sim 20\%$ shortening. At the early stages of shortening, tensile stresses are only obtained for 10^{-23} m^2 . (d) σ'_3 at the limb of the fold show tensile stresses at the early stages of shortening (0–2%) for the lowest permeability, but stresses remain compressive for all other permeabilities considered.

The stress evolution at the fold hinge (Figure 5c) shows the same trend for all scenarios whereby initially σ'_3 magnitudes increase to reach a maximum value at around 15–16% shortening and then drop significantly to reach a minimum at 25–30% shortening. Since the pore pressure for permeabilities of 10^{-13} to 10^{-17} m^2 remains hydrostatic variations of σ'_3 are negligible and tensile stresses are not reached at the hinge of the fold. As indicated by the evolution of overpressure for permeabilities of 10^{-19} to 10^{-23} m^2 σ'_3 magnitudes

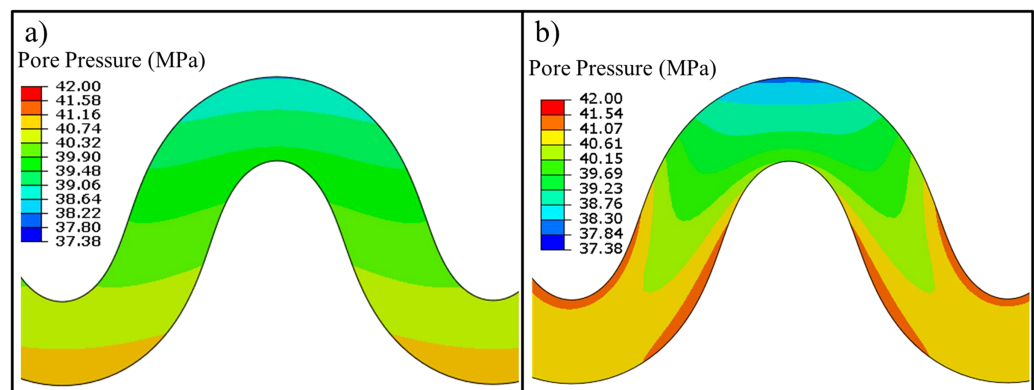


Figure 6. (a) Pore pressure magnitudes for 10^{-21} m^2 exhibits depth related relation with maximum and minimum values occurring at the bottom of the synform and top of the hinge, respectively. (b) Pore pressure magnitude for 10^{-23} m^2 are not depth related but linked to the strain distribution with the maximum pore pressure occurring in the limb.

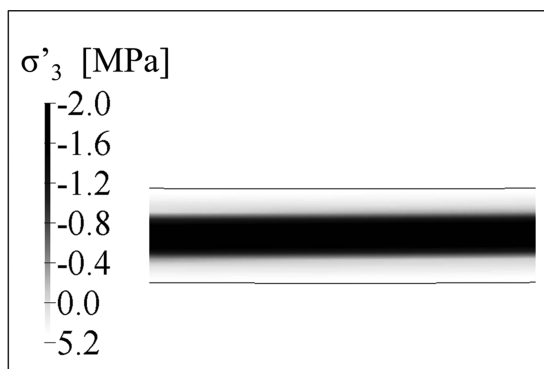


Figure 7. (a) σ'_3 for the lowest permeability model (10^{-23} m^2) during the initial 1% of shortening show minor tensile stresses of $\sim -2 \text{ MPa}$ (dark gray contours) for the middle of the layer.

are much lower and minimum tensile stresses of -3 to -8 MPa occur. It is important to note that the lowest σ'_3 magnitudes are obtained for $k=10^{-21} \text{ m}^2$ instead of the lowest permeability 10^{-23} m^2 due to the pore pressure distribution as discussed. σ'_3 magnitudes at the limb of the fold (Figure 5d) do not show significant variations after 5% of shortening and reach steady values. Only in the first 1–2% of shortening for the lowest permeability of 10^{-23} m^2 tensile stresses are attained initially. The σ'_3 magnitude results for 10^{-21} m^2 and 10^{-23} m^2 show that the dependency on permeability, especially after $\sim 16\%$ shortening, is both nonlinear and nonuniform. This behavior

can be explained by the pore pressure evolution (Figure 6). With respect to the development of tensile stresses, the case with the lowest permeability (10^{-23} m^2) merits further consideration (Figure 7). During the very early stages of deformation (0–1% shortening), minor tensile stresses (-1 to -3 MPa) are developed in the middle section of the layer. It is interesting to note that this behavior is not observed for the cases with permeabilities higher than 10^{-23} m^2 .

3.1.4.1. Permeability versus Overburden

In order to study the relative influences of the initial overburden pressure and permeability, Figure 8 shows the evolution of σ'_3 magnitudes for the various permeabilities considered for a low initial overburden thickness of 500 m. The σ'_3 results (Figure 8) show exactly the same trend as developed in the initial 1000 m overburden model, but tensile stresses are obtained for all permeabilities. For the lowest permeability (10^{-23} m^2), tensile stresses are also observed in the early stages of folding (0–2% shortening) at the limb. These results clearly show the influence of the overburden load as the major contributor controlling the magnitude and orientation of the compressional stress.

4. Discussion

The 2-D plane strain modeling approach presented in this paper shows that the stress history during the development of viscoelastic single-layer buckle folds can be successfully simulated and help provide a better understanding of the initiation and occurrence of tensile failure often seen in folded outcrops [e.g., *Bergbauer and Pollard, 2004; Reber et al., 2010*]. A large variety of studies explain the occurrence of tensile fractures at the hinge zone of the fold due to layer parallel tensional strain above a neutral surface. An important drawback of strain-based approaches, as stated by *Smart et al. [2009]*, is the neglect of gravity

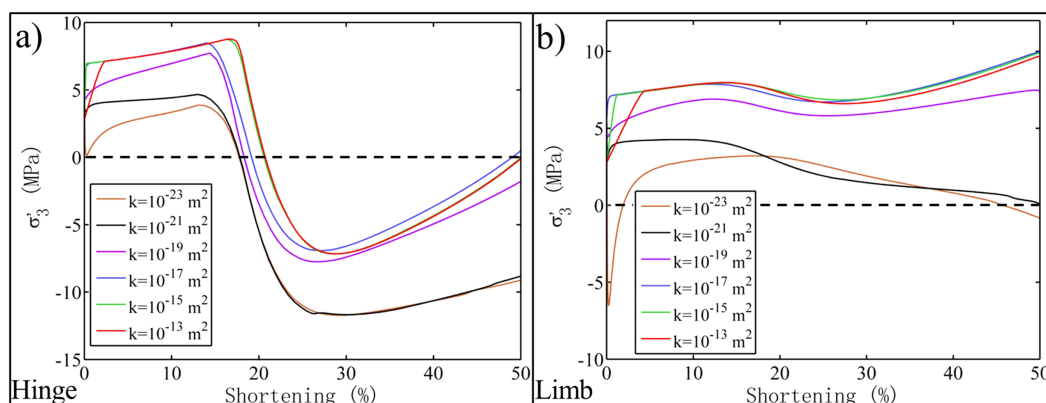


Figure 8. Permeability versus shortening for a model with a lower initial overburden load (500 m) for the hinge (a) and limb (b). The results show that the overburden is responsible for the overall degree of compression. Stress magnitudes at the hinge are much lower (compare with Figure 5) and tensile magnitudes (below dashed black line) are much more prevalent.

and pore pressure which prevents the analysis of tensile failure initiation using a failure criterion based on realistic stress magnitudes. While layer parallel and perpendicular strain may become tensile in curvature-based modeling approaches, the in situ state of stress is compressive and tensile buckling stresses need to be very large to overcome the compressional state of stress generated by the weight of the overburden. This study utilizes a modeling approach which simulates the buckling process under realistic in situ stress and strain conditions and the sensitivity analyses of the tested model parameters (overburden, competence contrast, viscosity, permeability) shows that tensile failure associated to the physical process of buckling may only be initiated under specific conditions. The results presented show that either low overburden pressures and/or high viscosities ($>5 \times 10^{21}$ Pa s) are required to initiate tensile failure at the hinge of buckle folds during their development. For the latter condition, the elastic response of the model is more dominant [Schmalholz and Podladchikov, 1999] resulting in lower (i.e., tensile) σ'_3 magnitudes and larger differential stresses at the hinge. Furthermore, the modeling results clearly demonstrate the governing role that permeability has on controlling the pore pressure, and hence effective stress conditions, within the folding layer and matrix. When significant overpressure development occurs, tensile failure in the fold hinge zone is more likely. The findings presented here agree with Lemiszki *et al.* [1994] who, based on Dieterich and Carter's [1969] results, conclude that tensile failure initiation in the outer arc of fold hinges can be predicted for a combination of the parameters of strain rate, overburden, pore pressures, and viscosity.

Lemiszki *et al.* [1994] conclude that folding at depths of more than 3000 m requires significant overpressures ($\lambda=0.73$) to explain tensile failure initiation. One drawback in Lemiszki *et al.*'s [1994] study is the numeric addition of pore pressure to Dieterich and Carter's [1969] model results. Our study shows that the development of overpressure during the folding process is closely linked to permeability and that values of $k \leq 10^{-19}$ m² are required to generate the fluid pressures needed to initiate tensile failure at a reference depth of 1232 m. For higher permeability rocks such as drained sandstones and carbonates, overpressure is either absent or of a minor magnitude and tensile failure is only likely for low overburden pressures or high viscosities ($>10^{21}$ Pa s).

For the situations where modeling results predict tensile failure, fractures parallel to the fold axis at the top of the hinge zone of the fold are expected. Tensile failure is only initiated after significant amount of shortening is applied ($>20\%$) and fold amplitudes are large, which is in agreement with findings of Reber *et al.* [2010].

The example model of single-layer fold scenarios used for this study shows that by using realistic sedimentary rock parameters folding-related fractures as shown in Figure 1 cannot in a general fashion be explained by the process of buckling alone. Furthermore, tensile failure observed on limbs of folds either perpendicular or parallel to the fold axis [e.g., Silliphant *et al.*, 2002; Bergbauer and Pollard, 2004] cannot be explained by the process of buckling when the influence of gravity is included. The modeling results also show that tensile failure parallel to the bedding planes only occurs for very low permeability scenarios in the initial stages of horizontal compression.

Since the conditions necessary for tensile failure during buckle folding determined in the sensitivity analyses described above do not provide a general explanation for the formation of tensile fractures linked to buckling (including for high permeability rocks) and fail to explain tensile failure in the limbs of folds, this study raises the question of what other processes and parameters play an important role in the initiation of tensile failure at depth. If tensile failure is not occurring during buckling, what is a likely cause for the commonly observed joint sets? Furthermore, is it possible for tensile failure to occur in folds at significant depths? The two most obvious possibilities are that (1) joints are present prefolding as suggested by Bergbauer and Pollard [2004] caused by overpressure development during sedimentation [Price and Cosgrove, 1990]; (2) joints are a post buckling phenomena and are the result of erosion and exhumation [e.g., Price, 1966; Hancock and Engelder, 1989; Bourne, 2003].

4.1. Erosion/Exhumation

Numerical modeling has been used by the authors to test the idea that the processes of erosion and exhumation which occur after the horizontal buckling compression has ceased, can result in the generation of tensile fractures. Erosion and exhumation effectively reduce the weight of the overburden and thus reduce the degree of compression within the fold structure. The resulting stress changes are investigated. For this purpose, an elastic load step following the horizontal shortening is applied, during which the weight of the

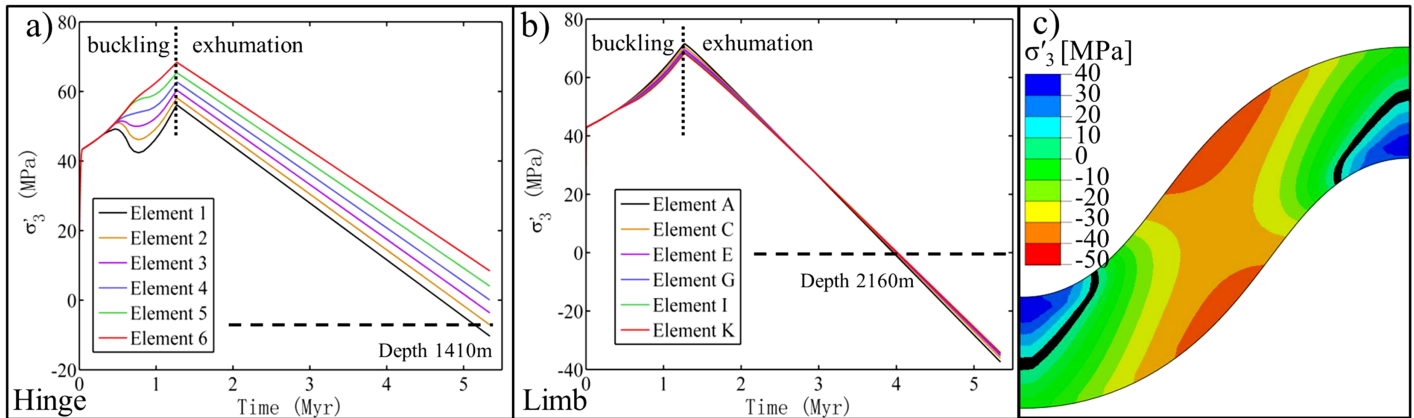


Figure 9. (a) σ'_3 magnitudes during the erosional unloading for the high permeability model (10^{-15} m^2) at the hinge of the fold. The results show that tensile stresses are obtained for elements 1–4 even with a significant overburden load remaining. For example, tensile stresses occur at Element 1 with an overburden of 1410 m. (b) σ'_3 magnitudes during the erosional unloading for the limb of the fold show uniform decrease toward tensile magnitudes. Tensile stresses occur at Element F with an overburden of 2160 m. (c) σ'_3 magnitudes after 4.07 Ma of exhumation showing tensile stresses at the top of the hinge and all across the limb of the fold. The black line separates compressive from tensile stresses.

overburden is reduced over geologically reasonable time scales. An erosion/exhumation rate of 1 mm/yr [Burbank, 2002] is considered by linearly reducing the magnitude of the gravitational acceleration for the overburden over a period of 4.07 Ma. The lateral model boundary conditions preserve the state of shortening and only vertical in-plane displacements are enabled. Two different scenarios are considered: (1) a high permeability case ($k = 10^{-15} \text{ m}^2$) with an initial overburden thickness of 3000 m and 40% shortening; and (2) a low permeability model ($k = 10^{-23} \text{ m}^2$) with an initial overburden thickness of 3000 m.

The validity of this approach is shown in supporting information Figure S1 where erosional unloading of a horizontally layered model matches the analytical solution given by [Turcotte and Schubert, 2002].

4.1.1. High Permeability

The results for the high permeability model (Figure 9a) show that while initial σ'_3 magnitudes at the fold hinge are compressive (56–74 MPa; after buckling), the erosion process causes the minimum principal stress σ'_3 to become tensile after 4.71 Ma for element 1, after 4.9 Ma for element 2, after 5.11 Ma for element 3, and after 5.34 Ma for element 4. Stresses in the limb of the fold (Figure 9b) show a similar trend and tensile stresses are obtained for all elements across the layer after 3.96 Ma. It is interesting to note that the resulting stress due to the removal of overburden ($\bar{\sigma}'_3$) does not follow the equation for uniaxial strain conditions [Turcotte and Schubert, 2002]:

$$\bar{\sigma}'_3 = \sigma'_3 - \frac{\nu}{1-\nu} \Delta\sigma'_1 \quad (11)$$

Eroding 4070 m of overburden and using equation (11) would result in a reduction, i.e., $\bar{\sigma}'_3 - \sigma'_3$ of 19.96 MPa in a horizontally layered model. Figure 9a shows that over 4.07 Ma σ'_3 is reduced by 66.45 MPa at Element 1. The remaining overburden at the onset of tensile stresses is 1410 m at the hinge and 2160 m at the limb of the fold. Thus, the reduction in overburden compression results in an amplification of the stresses due to buckling.

Figure 9c shows the contour plot of σ'_3 . The black line separates the compressive and tensile stress regimes. These results show that tensile stresses are localized at the hinge zone but that a much larger effect (i.e., much lower magnitudes) develops on the limbs. Here, tensile failure is widespread and the compressional stresses are relieved across the complete layer. This observation is similar to Fehner's [2011] results where tension occurs across the limbs at similar deformation stages (36% compared to 40% here). It should be noted that Fehner's [2011] modeling results are based on the state of strain in a buckle fold neglecting gravity. However, the similarity of the spatial distribution of tensional strain (Fehner's study) to tensional stresses after erosion (this study) fortifies the conclusion that the reduction in overburden compression (modeled as an elastic process) results in an amplification of the buckling stresses due to the remnant strain

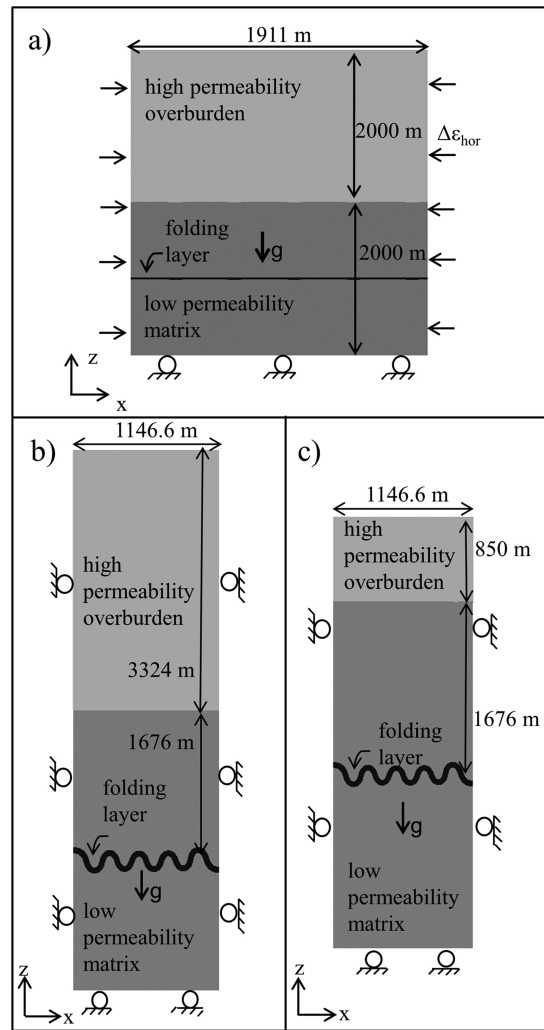


Figure 10. (a) Updated model setup for the low-permeability study. The folding layer is embedded in a 2000 m thick low permeability matrix. The remaining overburden has a high permeability. This enables the application of a zero pore pressure boundary condition at the top of the model during the erosional load step. (b) Model geometry and dimensions after 40% shortening. (c) Model geometry after erosional load step. Note model dimensions in Figure 10 are not to scale.

pressure history of the fold system has to be analyzed. While pore pressure for the high permeability zone remains hydrostatic (red line in Figure 11c), significant overpressure is generated during the compression load step in the low permeability part. At the onset of erosion, this overpressure is significantly reduced at a much higher rate than the hydrostatic section (Figure 11c). This behavior can be explained by observations from 1-D consolidation studies based on linear elastic deformation, whereby erosion (i.e., unloading) results in under pressure [Jiao and Zheng, 1998; Ellis and Darby, 2005]. Comparing the total stress evolution for the two permeability scenarios (supporting information Figures S2a and S2b), it is clear that σ_3 is approximately equal across the fold hinge (with slight differences at the bottom of the hinge) for the same exhumation time, indicating that the total stress is independent of the permeability. Figure 11 and supporting information Figure S2 show that the decrease in pore pressure and total stresses are approximately equal. This results in constant values for σ'_3 for the low permeability scenario. Hence, tensile stresses are not obtained due to erosional unloading.

4.2. Stress Orientation and Tensile Fractures

With the addition of the erosional load step, tensile stresses are developed at the hinge and throughout the limbs. To further investigate the significance of the initiation of tensile failure within the fold layer, we

stored in the folded layer and the results are thus similar to *Frehner's* [2011] study in which gravity is neglected.

4.1.2. Low Permeability

In order to test the influence of erosion in a low permeability model, the model setup is modified slightly (Figures 10a–10c). The folding layer is embedded in a 2000 m thick low permeability matrix ($k = 10^{-23} \text{ m}^2$). The overburden (2000 m) is assigned a high permeability (10^{-15} m^2) to simulate hydrostatic pore pressure decrease during the erosional unloading. This approach is necessary as the changing top of the model (Figure 10c) is assigned zero pore pressure, a boundary condition which does not yield reliable results if the overburden also has a low permeability.

The low permeability model shows a significant difference to the high permeability model when subjected to the erosional load step. σ'_3 magnitudes for both the hinge (Figure 11a) and the limb (Figure 11b) after the onset of erosion initially decrease slightly and then reach constant values. In order to understand this behavior, the pore

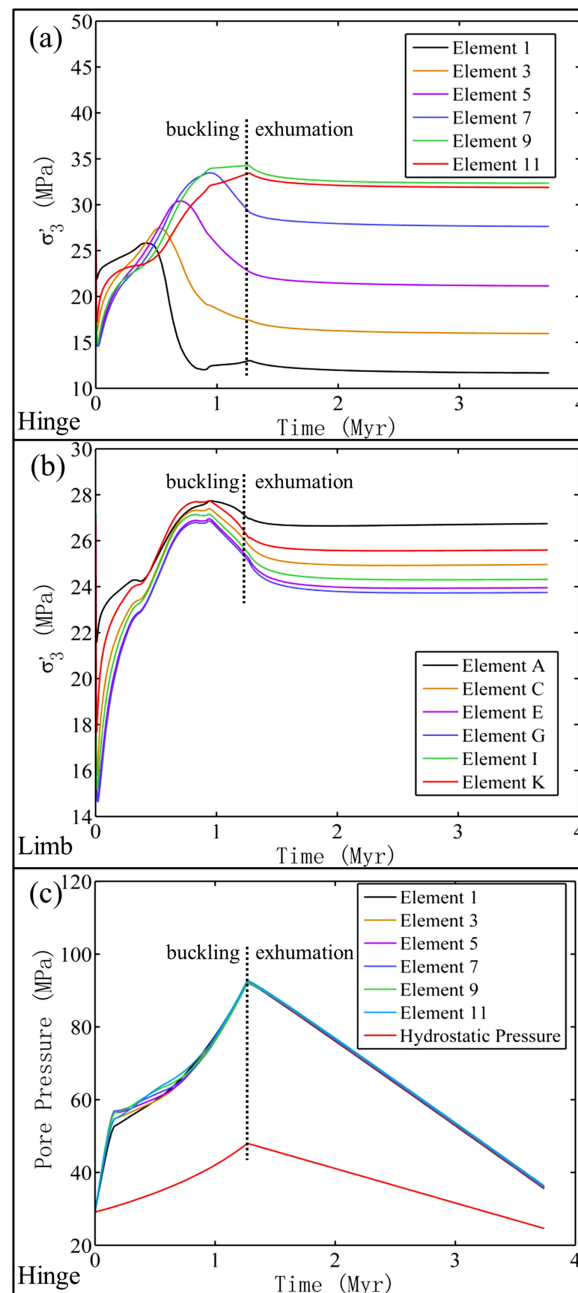


Figure 11. (a) σ_3 magnitudes during the erosional unloading for the low-permeability model (10^{-23} m^2) at the hinge of the fold. The results show a slight initial decrease is followed by σ_3 reaching constant magnitudes. Tensile stresses are not obtained. (b) σ_3 magnitudes at the limb of the fold display the same behavior. (c) The pore pressure decrease on the hinge during exhumation is much larger than the hydrostatic decrease (red line).

to the fold axis and perpendicular to the bedding (Figure 12c). These findings explain the occurrence of fracture Set 6 on Figure 1 in the limb and at the top of the hinge of buckle folds. Fracture Set 5 of Figure 1 cannot be generally explained by the modeling results. The out-of-plane principal stress in the 2-D modeling results becomes tensile at the top of the hinge for the low permeability ($<10^{-21} \text{ m}^2$), low initial overburden (500 m) scenario but remains compressive for all other cases (supporting information Figure S3). Unfortunately, the present modeling results cannot confirm *Reber et al.*'s [2010] conclusion that, based on the history of stress orientations during folding, vertical fractures in the fold limbs perpendicular to the fold axis (i.e., Set 5 in Figure 1) form at low fold amplitudes under layer-subparallel compression. In the 2-D plane strain model, the out-of-plane principal stress during the early stages is always compressive (supporting

examine the location, magnitude and orientation of tensile stresses during the load history, and determine the location and orientation of the tensile fractures that might form. Figure 12 shows the different scenarios and lists the conditions for tensile failure to occur during the load histories considered. During the early stages of horizontal compression for low permeability rocks (10^{-23} m^2), tensile failure is bedding parallel and occurs across the layer for all elements (Figure 12a). This can be attributed to the significant degree of overpressure being generated during the early stages of shortening. The pore pressure overcomes the vertical stress and separates the bedding planes. This phenomenon is commonly observed in shale formations [Cosgrove, 2001; Cobbold et al., 2013 and references therein]. For the later stages of buckling, tensile failure in low permeability rocks ($<10^{-19} \text{ m}^2$) occurs at the hinge and the fractures are normal to bedding and parallel to the fold axis (Figure 12b). This type of failure is also possible for high permeability rocks having low overburden pressures and/or high viscosities. In addition, for high permeability rocks tensile failure can be observed during erosional unloading. Vertical fractures parallel to the fold axis occur at the hinge and tensile fractures in the limb are oriented parallel

	Conditions	Tensile failure orientation and location
(a)	Low permeability (during early stages of buckling)	
(b)	Low overburden and/or high viscosity and/or low permeability	
(c)	High permeability (during erosional unloading)	

Figure 12. Orientation of tensile failure (red lines) for different model scenarios and the conditions for their occurrence. The black lines represent the orientations of σ_3 . The darker gray contours show the spatial extent of tensile stress magnitudes. (a) During the early stages of buckling for low the permeability scenario, tensile failure is bedding parallel and perpendicular to the fold axis. (b) During the later stages of buckling, tensile fractures occur at the top of the hinge parallel to the fold axis and perpendicular to the bedding. Conditions for this type of failure are low overburden pressure and/or high-layer viscosity or low permeability ($<10^{-19} \text{ m}^2$). (c) For high permeability rocks ($>10^{-16} \text{ m}^2$), tensile failure occurs during erosional unloading and is widespread across the limb with orientations parallel to the fold axis and perpendicular to bedding. Tensile failure also occurs at the top of the hinge.

information Figure S3) and does not promote the initiation of vertical tensile fractures perpendicular to the fold axis. It should be noted that *Reber et al.*'s [2010] observation is based on a large competence contrast of $R_{\mu} = 100$ and that they also conclude that for significant overburden pressures tensile failure is unlikely.

4.3. Limitations

It is clear that by utilizing a 2-D plane strain approach for simulating single-layer viscoelastic buckle folds model limitations arise. The plane strain approach effectively limits the analysis to the in-plane principal stresses and therefore a detailed analysis of tensile stresses in the direction of the out-of-plane principal stress is restricted. While the out-of-plane principal stress becomes tensile in the late deformation stages for the low permeability, low overburden scenario, a detailed analysis requires a 3-D

modeling approach. Stress magnitudes in this direction are directly dependent on the boundary conditions in that dimension, i.e., whether the model is constrained, compressed, or extended in the third dimension.

One of the most important limitations of the models presented is the omission of plastic deformation. Once tensile stresses of about 5–10 MPa are reached most sedimentary rocks fail and stresses are not increasing. Moreover, tensile failure will be accompanied by an increase in permeability creating a tendency to nullify the development of tensile stresses. However, the main objective of this study is to focus on and pinpoint the spatial and temporal occurrence of tensile stresses which are necessary for the onset of tensile failure. Therefore, the development of tensile effective stresses is considered a reasonable indicator of the initiation of tensile failure in the models and their natural counterparts. The subsequent yield behavior and further evolution of tensile failure is beyond the scope of this study and requires a different approach involving a plastic constitutive relationship.

In an attempt to determine the impact of permeability on the stress state that develops within the model, a homogeneous distribution of permeability throughout the model domain is assumed. The authors have, however, also tested the influence of a heterogeneous permeability distribution in the model. These results show that the matrix permeability is the major factor controlling the stress magnitudes in the model.

In the models involving the erosional load step isothermal processes are assumed and thus thermal stresses due to cooling during exhumation/erosion are not included. Clearly, the addition of a changing temperature field (particularly for high geothermal gradient regions) as well as more detailed analyses of the pore pressure evolution with respect to permeability and overburden thickness is required in order to investigate specific geological scenarios. These specific features are beyond the scope of this paper, but are very tractable using the methodology presented. Last, detailed understanding of a structure's strain history is necessary in order that a robust comparison of the numerical results and field observations can be made.

5. Conclusions

An extensive 2-D plane strain numerical modeling study of viscoelastic single-layer buckle folding has shown that tensile stresses and associated tensile failure only occurs under special conditions. It is concluded that the buckling process determines the strain distribution within the fold layer but is not solely responsible for the occurrence of tensile stresses. While buckling results in regions of compression at the bottom of the fold hinge (i.e., in the inner arc) and extension in the outer arc of the fold hinge, this study shows that parameters such as overburden thickness, viscosity, competence contrast, and most importantly permeability have a governing influence on the absolute magnitude of the least effective principal stress, σ'_3 . With respect to their relative impact on σ'_3 magnitudes, the results presented here show:

1. The competence contrast, R_{μ} , between matrix and fold layer determines the magnitude of buckling (i.e., fold amplitude and onset of buckle process). A lower R_{μ} results in lower amplitude folds and higher σ'_3 magnitudes. A higher R_{μ} results in larger amplitude folds and lower σ'_3 magnitudes. The higher R_{μ} , the earlier the buckling process results in a decrease in σ'_3 magnitudes at the hinge of the fold.
2. For high viscosities ($>10^{21}$ Pa s), the elastic influence on the deformation is increased and tensile stresses are more likely.
3. The initial overburden thickness determines the amount of compression in the model. Lower overburden pressure promotes the onset of tensile failure. Higher overburden pressures decreases the likelihood of tensile stresses and failure at depth.
4. Permeability is a crucial factor with respect to the generation of compression associated overpressure and σ'_3 magnitudes. Rocks with a permeability of 10^{-19} m² and smaller exhibit overpressure and tensile stresses at the hinge of the fold after $\sim 20\%$ shortening. Only for the lowest permeability tested (10^{-23} m²) are tensile stresses observed in the limb of the fold in the early stages of buckling.

Based on the buckling process, we conclude that tensile stresses in the hinge are likely at depth for high viscosity, low overburden, or for cases with low permeability ($<10^{-19}$ m²). Tensile failure becomes more likely the lower the overburden pressure. Tensile fractures (at the hinge) forming in these stress conditions are parallel to the fold axis (i.e., vertical). Tensile stresses in the limb of the fold cannot be generally explained by single-layer buckling. Only for extremely low permeabilities (10^{-23} m²) can tensile stresses be observed in the early stages of deformation and result in bedding parallel layer separation.

Erosional unloading has a significant impact on the state of stress within a buckle fold. For high permeability rocks ($k > 10^{-16}$ m²), the pore pressure remains hydrostatic during all load steps and erosion results in the generation of significant tensile stresses throughout the fold structure. The results presented show that erosion of high permeability rocks can explain the generation of tensile stresses at significant depths (1.4–2.2 km) both at the hinge of the fold and throughout its limbs. Tensile fractures in the limb are oriented parallel to the fold axis and perpendicular to the bedding. For low permeability rocks ($k < 10^{-16}$ m²), erosional unloading results in constant σ'_3 magnitudes as the pore pressure drops significantly. This pore pressure equilibration process decreases the likelihood of tensile stresses evolving.

The results of this study show that tensile stresses and associated failure within buckle folds is directly dependent on the distribution of material parameters but moreover to the strain history of the geologic system.

Acknowledgments

This work was supported and funded by Chevron ETC. Their permission to publish this work is gratefully acknowledged. We would like to thank John Cosgrove and three anonymous reviewers for their valuable and constructive reviews, which greatly improved the manuscript. The data for this paper are available at the Department of Geosciences and Geological and Petroleum Engineering at Missouri University of Science and Technology by contacting the corresponding author.

References

- Bai, T., and D. D. Pollard (2000), Fracture spacing in layered rocks: a new explanation based on the stress transition, *J. Struct. Geol.*, 22(1), 43–57, doi:10.1016/S0191-8141(99)00137-6.
- Bergbauer, S., and D. D. Pollard (2004), A new conceptual fold-fracture model including prefolding joints, based on the Emigrant Gap anticline, Wyoming, *Geol. Soc. Am. Bull.*, 116(3-4), 294–307, doi:10.1130/B25225.1.
- Biot, M. A. (1961), Theory of folding of stratified viscoelastic media and its implications in tectonics and orogenesis, *Geol. Soc. Am. Bull.*, 72, 1595–1620.
- Bourne, S. J. (2003), Contrast of elastic properties between rock layers as a mechanism for the initiation and orientation of tensile failure under uniform remote compression, *J. Geophys. Res.*, 108(B8), 2395, doi:10.1029/2001JB001725.
- Buchmann, T. J., and P. T. Connolly (2007), Contemporary kinematics of the Upper Rhine Graben: A 3D finite element approach, *Global Planet. Change*, 58(1), 287–309, doi:10.1016/j.gloplacha.2007.02.012.
- Burbank, D. W. (2002), Rates of erosion and their implications for exhumation, *Mineralogical Magazine*, 66(1), 25–52, doi:10.1180/0026461026610014.
- Casey, M., and R. W. Butler (2004), Modelling approaches to understanding fold development: implications for hydrocarbon reservoirs, *Mar. Pet. Geol.*, 21(7), 933–946, doi:10.1016/S0264-8172(04)00063-7.

- Chapple, W. M., and J. H. Spang (1974), Significance of layer-parallel slip during folding of layered sedimentary rocks, *Geol. Soc. Am. Bull.*, *85*(10), 1523–1534.
- Cobbold, P. R., A. Zanella, N. Rodrigues, and H. Loseth (2013), Bedding-parallel fibrous veins (beef and cone-in-cone): Worldwide occurrence and possible significance in terms of fluid overpressure, hydrocarbon generation and mineralization, *Mar. Pet. Geol.*, *43*(5), 1–20.
- Cooke, M. L., and C. A. Underwood (2001), Fracture termination and step-over at bedding interfaces due to frictional slip and interface opening, *J. Struct. Geol.*, *23*(2), 223–238, doi:10.1016/S0191-8141(00)00092-4.
- Cosgrove, J.W. (2001), Hydraulic fracturing during the formation and deformation of a sedimentary basin; its role in the dewatering of low permeability sediments. *AAPG Bull.* *85*, 737–748.
- Dieterich, J. H., and N. L. Carter (1969), Stress-history of folding, *Am. J. Sci.*, *267*(2), 129–154.
- Eckert, A., and P.T. Connolly (2007), Stress and fluid-flow interaction for the Coso Geothermal Field derived from 3D numerical models, *Trans. Geotherm. Resour. Counc.*, *31*, 385–390.
- Ellis, S., and D. Darby (2005), A modified Terzaghi consolidation factor for first-order estimation of overpressure resulting from sedimentation: review and synthesis, *Math. Geol.*, *37*(1), 115–123, doi:10.1007/s11004-005-8750-0.
- Ericsson, J. B., H. C. McKean, and R. J. Hooper (1998), Facies and curvature controlled 3D fracture models in a Cretaceous carbonate reservoir, Arabian Gulf, *Geol. Soc. Spec. Publ.*, *147*(1), 299–312, doi:10.1144/GSL.SP.1998.147.01.20.
- Fischer, M. P., and M. S. Wilkerson (2000), Predicting the orientation of joints from fold shape: Results of pseudo-three-dimensional modeling and curvature analysis. *Geology*, *28*(1), 15–18.
- Frehner, M. (2011), The neutral lines in buckle folds, *J. Struct. Geol.*, *33*(10), 1501–1508, doi:10.1016/j.jsg.2011.07.005.
- Hancock, P. L., and T. Engelder (1989), Neotectonic joints, *Geol. Soc. Am. Bull.*, *101*(10), 1197–1208.
- Hennings, P. H., J. E. Olson, and L. B. Thompson (2000), Combining outcrop data and three-dimensional structural models to characterize fractured reservoirs: An example from Wyoming. *AAPG Bull.*, *84*(6), 830–849.
- Jaeger, J. C., N. G. Cook, and R. W. Zimmerman (2007), *Fundamentals of Rock Mechanics*, pp. 116–185, Blackwell, Oxford, U. K.
- Jeng, F. S., and K. P. Huang (2008), Buckling folds of a single layer embedded in matrix—Theoretical solutions and characteristics, *J. Struct. Geol.*, *30*(5), 633–648, doi:10.1016/j.jsg.2008.01.009.
- Jeng, F. S., M. L. Lin, Y. C. Lai, and M. H. Teng (2002), Influence of strain rate on buckle folding of an elasto-viscous single layer, *J. Struct. Geol.*, *24*(3), 501–516, doi:10.1016/S0191-8141(01)00073-6.
- Jiao, J. J., and C. Zheng (1998), Abnormal fluid pressures caused by deposition and erosion of sedimentary basins, *J. Hydrol.*, *204*(1), 124–137, doi:10.1016/S0022-1694(97)00115-7.
- Johnson, A. M., and R. C. Fletcher (1994), *Folding of Viscous Layers: Mechanical Analysis and Interpretation of Structures in Deformed Rock*, pp. 188–267, Columbia Univ. Press, N. Y.
- Lemiszki, P. J., J. D. Landes, and R. D. Hatcher (1994), Controls on hinge-parallel extension fracturing in single-layer tangential-longitudinal strain folds, *J. Geophys. Res.*, *99*(B11), 22,027–22,041, doi:10.1029/94JB01853.
- Lisle, R. J. (1994), Detection of zones of abnormal strains in structures using Gaussian curvature analysis, *AAPG Bull.*, *78*(12), 1811–1819.
- Mancktelow, N.S. (1999), Finite-element modeling of single-layer folding in elasto-viscous materials: The effect of initial perturbation geometry, *J. Struct. Geol.*, *21*, 161–177, doi:10.1016/S0191-8141(98)00102-3.
- Mancktelow, N.S. (2008), Tectonic pressure: Theoretical concepts and modelled examples, *Lithos*, *103*(1–2), 149–177, doi:10.1016/j.lithos.2007.09.013.
- McQuillan, H. (1973), Small-scale fracture density in Asmari Formation of southwest Iran and its relation to bed thickness and structural setting, *AAPG Bull.*, *57*(12), 2367–2385.
- Medina C.R., J. A. Rupp, and D. A. Barnes (2011), Effects of reduction in porosity and permeability with depth on storage capacity and injectivity in deep saline aquifers: A case study from the Mount Simon Sandstone aquifer, *Int. J. Greenh. Gas Control*, *5*(2011), 146–156, doi:10.1016/j.ijggc.2010.03.001.
- Narr, W., and J. Suppe (1991), Joint spacing in sedimentary rocks. *J. Struct. Geol.*, *13*(9), 1037–1048, doi:10.1016/0191-8141(91)90055-N.
- Price, N. J. (1966), *Fault and Joint Development in Brittle and Semi-Brittle Rock*, vol. 1, pp. 1–52, Pergamon, Oxford, U. K.
- Price, N. J. (1974), The development of stress systems and fracture patterns in undeformed sediments, in *Advances in Rock Mechanics, Proceedings of the 3rd Conference ISRM*, Denver, vol. 1, pp. 487–496, Natl. Acad. Sci., Washington, D. C.
- Price, N. J., and J. W. Cosgrove (1990), *Analysis of Geological Structures*, Cambridge Univ. Press, U. K.
- Ramsay, J. G. (1967), *Folding and Fracturing of Rocks*. McGraw-Hill, N. Y.
- Ramsay, J. G., and Y. Huber (1987), *The Techniques of Modern Structural Geology, vol. 2, Folds and Fractures*, pp. 641–665, Academic, London, U. K.
- Ranalli, G. (1995), *Rheology of the Earth*, pp. 84–86, Chapman and Hall, London, U. K.
- Reber, J. E., S. M. Schmalholz, and J. P. Burg (2010), Stress orientation and fracturing during three-dimensional buckling: Numerical simulation and application to chocolate-tablet structures in folded turbidites, SW Portugal, *Tectonophysics*, *493*(1), 187–195, doi:10.1016/j.tecto.2010.07.016.
- Schmalholz, S. M. (2008), 3D numerical modeling of forward folding and reverse unfolding of a viscous single-layer: Implications for the formation of folds and fold patterns, *Tectonophysics*, *446*(1), 31–41, doi:10.1016/j.tecto.2007.09.005.
- Schmalholz, S. M., and Y. Podladchikov (1999), Buckling versus folding: importance of viscoelasticity, *Geophys. Res. Lett.*, *26*(17), 2641–2644, doi:10.1029/1999GL900412.
- Schmalholz, S. M., Y. Y. Podladchikov, and D. W. Schmid (2001), A spectral/finite difference method for simulating large deformations of heterogeneous, viscoelastic materials, *Geophys. J. Int.*, *145*, 199–208, doi:10.1046/j.0956-540x.2000.01371.x.
- Schmalholz, S. M., Y. Y. Podladchikov, and J. P. Burg (2002), Control of folding by gravity and matrix thickness: Implications for large-scale folding, *J. Geophys. Res.*, *107*(B1), doi:10.1029/2001JB000355.
- Sibson, R. H. (1996), Structural permeability of fluid-driven fault-fracture meshes, *J. Struct. Geol.*, *18*(8), 1031–1042, doi:10.1016/0191-8141(96)00032-6.
- Silliphant, L. J., T. Engelder, and M. R. Gross (2002), The state of stress in the limb of the Split Mountain anticline, Utah: Constraints placed by transected joints, *J. Struct. Geol.*, *24*(1), 155–172, doi:10.1016/S0191-8141(01)00055-4.
- Smart, K. J., D. A. Ferrill, and A. P. Morris (2009), Impact of interlayer slip on fracture prediction from geomechanical models of fault-related folds, *AAPG Bull.*, *93*(11), 1447–1458, doi:10.1306/05110909034.
- Srivastava, D. C., and T. Engelder (1990), Crack-propagation sequence and pore-fluid conditions during fault-bend folding in the Appalachian Valley and Ridge, central Pennsylvania. *Geol. Soc. Am. Bull.*, *102*(1), 116–128.

- Stearns, D. W. (1968), Certain aspects of fracture in naturally deformed rocks, in: *NSF Advanced Science Seminar in Rock Mechanics, Spec. Rep. AD66993751*, edited by R. E. Riecker, pp. 97–118, Air Force Cambridge Res. Lab., Bedford, Mass.
- Stearns, D. W., and M. Friedman (1972), Reservoirs in fractured rock, *AAPG Memo.*, 16, 82–100.
- Stephansson, O. (1974), Stress-induced diffusion during folding, *Tectonophysics*, 22(3), 233–251.
- Turcotte, D. L., and G. Schubert (2002), *Geodynamics*, pp. 106–109, Cambridge Univ. Press, N. Y.
- Twiss, R. J., and E. M. Moores (2007), *Structural Geology*, 2nd ed., pp. 273–292, W. H. Freeman, N. Y.
- Zhang, Y., B. E. Hobbs, A. Ord, and H. B. Muhlhaus (1996), Computer simulation of single-layer buckling, *J. Struct. Geol.*, 18, 645–655, doi: 10.1016/S0191-8141(96)80030-7.
- Zhang, Y., N. S. Mancktelow, B. E. Hobbs, A. Ord, and H. B. Muhlhaus (2000), Numerical modeling of single-layer folding: Clarification of an issue regarding the possible effect of computer codes and the influence of initial irregularities, *J. Struct. Geol.*, 22, 1511–1522, doi: 10.1016/S0191-8141(00)00063-8.